JOURNAL OF SPACECRAFT AND ROCKETS
Vol. 45, No. 3, May–June 2008

Real-Time Navigation for Mars Missions Using the Mars Network

E. Glenn Lightsey* and Andreas E. Mogensen†
University of Texas at Austin, Austin, Texas 78712
and
P. Daniel Burkhart,‡ Todd A. Ely,‡ and Courtney Duncan‡
Jet Propulsion Laboratory, California Institute of Technology, Pasadena, California, 91109-8099

DOI: 10.2514/1.30974

A NASA Mars technology program task is developing a prototype, embedded, real-time navigation system for Mars final approach and entry, descent, and landing using the Mars Network's Electra ultrahigh frequency transceiver. The Mars Network is ideally situated to provide spacecraft-to-spacecraft navigation via the Electra ultrahigh frequency transceiver, which is a versatile telecommunications payload that is capable of providing autonomous on-orbit, real-time trajectory determination using two-way Doppler measurements between a Mars approach vehicle and a Mars Network orbiter. A set of analyses based on the 2010 encounter at Mars between the Mars Science Laboratory and the Mars Reconnaissance Orbiter demonstrate that the navigation system is capable of achieving a 300 m or better atmosphere entry knowledge error and that the resulting technology is a key component to enabling pinpoint landing. The development approach, software design, and test results from an engineering development unit are presented.

Nomenclature

a	=	clock acceleration or oscillator aging, $\mathrm{s/s^2}$
$\mathbf{a}_A$	=	acceleration measurement model of spacecraft acceleration in the accelerometer frame, $\mathrm{m/s^2}$
$\mathbf{a}_A^B$	=	true spacecraft acceleration vector in the body frame, $\mathrm{m/s^2}$
$\mathbf{a}_{\mathrm{cg,ng,mod}}^I$	=	spacecraft acceleration because of modeled nongravitational forces in the inertial frame, $\mathrm{m/s^2}$
B_R	=	bit rate, bps
B_W	=	filter bandwidth, Hz
b	=	clock bias, s
$\mathbf{b}_A$	=	vector of accelerometer biases per axis, $\mathrm{m/s^2}$
$\mathbf{b}_G$	=	vector of gyro biases per axis, rad/s
C/N_0	=	carrier power-to-noise density ratio
$c(t)$	=	clock time, cycles
d	=	clock drift, s/s
E_b/N_0	=	bit energy-to-noise density ratio
$\hat{\mathbf{e}}_r$	=	unit vector in the direction of the vector $\mathbf{r}$
$\mathbf{F}_{\mathrm{ng,dyn}}^I$	=	nongravitational forces acting on spacecraft center of gravity, N
f	=	frequency, Hz
G_t, G_r	=	gain of the transmitter and receiver
$\mathbf{g}_{\mathrm{cg}}^I$	=	gravitational acceleration acting on spacecraft center of gravity, $\mathrm{m/s^2}$
$\mathbf{H}_A$	=	accelerometer measurement partial derivatives
$\mathbf{J}_{\mathrm{SC}}$	=	spacecraft inertia matrix, $\mathrm{kg\,m^2}$
L/D	=	lift-to-drag ratio
L_i, L_s, L_p, L_r	=	losses in the signal transmit–receive path
$M_{(*)(*)}$	=	internal fundamental integer multipliers in the Electra transceiver and transponder
$\mathbf{M}_{\mathrm{MA}}$	=	3×3 matrix of axis misalignment errors (zero-diagonal matrix)
$\mathbf{M}_{\mathrm{NO}}$	=	3×3 matrix of nonorthogonality errors (zero-diagonal matrix)
M_{SC}	=	spacecraft mass, kg
$\mathbf{M}_{\mathrm{SF}}$	=	3×3 matrix of scale factor errors (diagonal matrix)
N	=	unknown phase ambiguity, rad
O^{2WID}	=	two-way integrated Doppler observable, rad
O^{2WTP}	=	two-way total count phase measurement, rad
P_{rt}	=	total received power, dBm
$\mathbf{r}$, r	=	position vector and magnitude of position vector, m
$\dot{\mathbf{r}}$, $\dot{r}$	=	velocity vector and magnitude of velocity vector, m/s
$\ddot{\mathbf{r}}$, $\ddot{r}$	=	acceleration vector and magnitude of acceleration vector, $\mathrm{m/s^2}$
$\mathbf{r}_{A/\mathrm{cg}}^B$	=	relative position vector of origin of A frame relative to spacecraft center of gravity, expressed in the B frame, m
T	=	Doppler count interval, s
$\mathbf{T}_B^I$	=	rotation matrix from frame B to frame I
t	=	time, s
$\mathbf{v}_{\mathrm{cg}}^I$	=	velocity vector of spacecraft center of gravity in the inertial frame, m/s
$\mathbf{X}_k$	=	state vector at time t_k
$\boldsymbol{\alpha}_{\mathrm{SC,mod}}^B$	=	spacecraft angular acceleration because of modeled torques in the body frame, $\mathrm{rad/s^2}$
$\boldsymbol{\alpha}_{\mathrm{SC,unmod}}^B$	=	unmodeled spacecraft angular acceleration in the body frame, $\mathrm{rad/s^2}$
Δ	=	time delay in the Electra signal transmit–receive path, s
Δf	=	Doppler shift, Hz
Δ_{2W}	=	Electra two-way signal delay, s
$\delta \boldsymbol{a}_{\mathrm{cg,unmod}}^B$	=	empirically estimated unmodeled acceleration acting on spacecraft center of gravity in the body frame, $\mathrm{m/s^2}$
$\boldsymbol{\varepsilon}_A$	=	vector of accelerometer random noise per axis, $\mathrm{m/s^2}$

Received 12 March 2007; revision received 5 August 2007; accepted for publication 8 August 2007. Copyright © 2007 by Caltech. Published by the American Institute of Aeronautics and Astronautics, Inc., with permission. Copies of this paper may be made for personal or internal use, on condition that the copier pay the $10.00 per-copy fee to the Copyright Clearance Center, Inc., 222 Rosewood Drive, Danvers, MA 01923; include the code 0022-4650/08 $10.00 in correspondence with the CCC.

*Associate Professor, Department of Aerospace Engineering and Engineering Mechanics, 1 University Station C0600. Associate Fellow AIAA.

†Graduate Student, Department of Aerospace Engineering and Engineering Mechanics, 1 University Station C0600. Student Member AIAA.

‡Senior Engineer, Guidance, Navigation, and Control Section, 4800 Oak Grove Drive, Mail Stop 301-125L. Senior Member AIAA.

$\boldsymbol{\varepsilon}_G$	=	vector of gyro random noise per axis, $\mathrm{m/s^2}$
ρ	=	round-trip light time, s
τ	=	measurement time tag
τ_a	=	unmodeled acceleration component random correlation time constant, s
$\boldsymbol{\tau}^I_{\mathrm{dyn}}$	=	torques acting on the spacecraft in the inertial frame, $\mathrm{N \cdot m}$
υ^{2WTP}	=	phase errors from sources other than the oscillator, such as thermal link noise and multipath, rad
$\Phi(t_i, t_{i-1})$	=	state transition matrix
ϕ	=	phase angle, rad
ψ	=	oscillator random phase process, rad
$\boldsymbol{\omega}$	=	angular velocity vector, rad/s
$\boldsymbol{\omega}_G$	=	gyro measurement model of spacecraft angular velocity vector in the gyro reference frame, rad/s
$\boldsymbol{\omega}^B_{\mathrm{SC}}$	=	true spacecraft angular velocity vector in the body reference frame, rad/s

Superscripts

B	=	body reference frame
G	=	gyro platform reference frame
I	=	inertial reference frame

Subscripts

A	=	accelerometer reference frame
cg	=	center of gravity
SC	=	spacecraft
t	=	transponder
x	=	transceiver

I. Introduction

THE Mars technology program at NASA has identified pinpoint landing as a key advanced entry, descent, and landing (EDL) technology for future Mars landers. Pinpoint landing is defined for the purposes of this discussion as landing within 1 km of a preselected target. Scientific goals for the next decade of Mars exploration (such as the search for water and characterization of the aqueous processes on Mars, the study of the mineralogy and weathering of the Martian surface, and the search for preserved biosignatures in Martian rocks) require placing landers at predefined locations of the greatest scientific interest [1]. The capability to land within 1 km of a predefined landing site will improve safety and enable landing within roving range of sites of scientific interest while avoiding hazardous areas.

For a guidance system to achieve pinpoint landing, precise trajectory knowledge is required. This is true, in particular, during the mission's final approach phase and EDL phase when the spacecraft is actively guiding itself. For the purposes of the technology effort, the final approach phase is defined as the period from 12 h before atmospheric entry up to the point just before entry at the top of the atmosphere. These mission phases are illustrated in Fig. 1. During the initial approach phase, accurate trajectory knowledge is useful for minimizing Mars targeting errors. Navigation during the initial approach phase is mostly an ground-based Earth activity because there is sufficient time to relay telemetry and uplink commands to the spacecraft. It is during the final and most critical mission phases that precise trajectory information provided to an onboard guidance system can be most useful for aiding pinpoint landing. However, the final mission phases are brief and must proceed without ground-based Earth support because of light–time delays. The implication is that trajectory knowledge updates past the ground-based data cutoff, which is typically 6 h before entry, must be obtained in situ and processed onboard.

The Mars Network is ideally situated to provide spacecraft-to-spacecraft radiometric navigation data that can be processed onboard the approaching spacecraft in real time during the final approach and

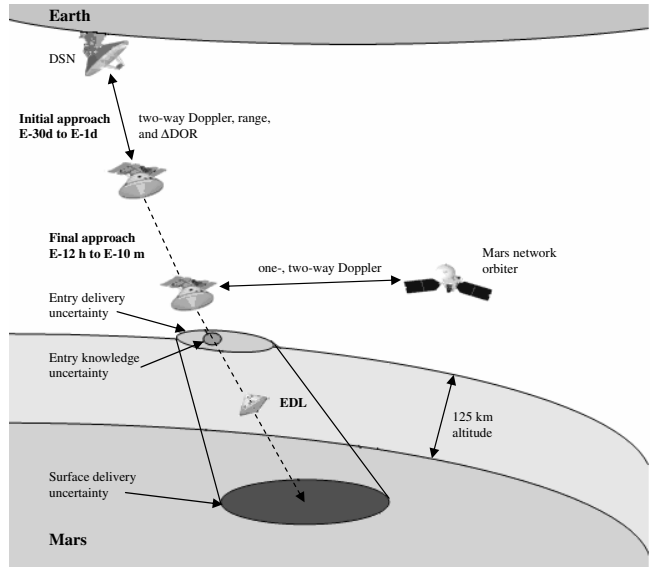

Fig. 1 The initial approach, final approach, and entry, descent, and landing phases of a Mars mission with radiometric tracking provided by the Mars Network.

EDL phases [2,3]. This will enable improvements in surface positioning error and improve the performance of entry guidance. Table 1 shows the performance of several navigation and guidance strategies for Mars landing [4]. The performance is given in terms of the size of the 3σ uncertainty ellipses. The current baseline strategy that uses only ground-based Earth radiometric data is represented in the first row, whereas an approach using Mars Network-based spacecraft-to-spacecraft radiometric data is represented in the second and third rows.

Note that in Table 1, entry knowledge uncertainty represents the trajectory uncertainty at the top of the atmosphere given the proposed tracking strategy stated in each row, whereas entry delivery uncertainty represents the trajectory uncertainty at the top of the atmosphere when the knowledge, up to a certain data cutoff time, is used with guidance. Also note that ballistic surface delivery represents an unguided entry, descent, and landing such as was used on the Mars Exploration Rover (MER) missions. Finally, hypersonic guidance represents guidance in the upper atmosphere, whereas hypersonic and chute guidance represents guidance in the upper atmosphere and guidance while on the parachute.

The landing system used for the MER mission, shown in Table 1 as the three cells containing bold characters, represents the current state of the art and yields final delivery errors at the top of the Mars atmosphere of 9 km. These errors grow to 80 km at the surface of Mars since the MER entry is ballistic. Even with active guidance during entry, as is the case for the Mars Science Laboratory (MSL) mission, the surface delivery errors are on the order of 10 km and cannot decrease to less than the entry errors without further navigation sensor data that could consist of either in situ radiometric tracking or optical navigation. In fact, achieving pinpoint landing accuracies of less than 1 km requires that the approaching spacecraft's guidance system has real-time trajectory updates at the same level of accuracy during final approach, unless the spacecraft has a significant fuel budget to allow for substantial maneuvers during EDL. Pinpoint landing that is aided by Mars Network navigation data during both the final approach and EDL and integrated with active guidance is shown in the last row of Table 1. The case illustrates that final approach navigation enables pinpoint landing for a system that minimizes fuel expenditures for maneuvers during EDL.

The Mars Network is capable of providing spacecraft-to-spacecraft navigation data using the Electra ultrahigh frequency (uhf) transceiver, which is manifested as baseline equipment for current and future Mars missions, including the Mars Reconnaissance Orbiter (MRO) that arrived at Mars in 2006. A key service of the Mars Network is to provide communications using the Electra

Table 1 Atmosphere entry and surface delivery errors of a Mars lander using Deep Space Network (DSN) tracking data only or DSN and Mars Network radiometric tracking for various guidance strategies

Radio navigation capability	3σ entry uncertainty ellipses, km		3σ surface delivery uncertainty ellipses, km			Comments
	Knowledge	Delivery	Ballistic (MER)	Hypersonic guided entry (MSL)	Hypersonic plus chute-guided entry	
1) Ground-based X-band DSN radio navigation (Doppler, range, ΔDOR), $E-18$ h data cutoff, $E-6$ h maneuver, trajectory update at $E-4$ h	**1.5×1.5**	**9×1.5**	**80×12**	10 × 5	10 × 5	Baseline tracking for the MER and the MSL. Chute guidance of no value without additional tracking.
2) Case 1 + S/C to S/C uhf-band Doppler using the Mars Network, autonomous processing begins at $E-10$ h, maneuver at $E-1$ h	*0.3 × 0.3*	0.3 × 0.3	38 × 5	3 × 3	3 × 3	Improved entry knowledge improves the MER and the MSL cases.
3) Case 2 + additional uhf data through EDL	0.3 × 0.3	0.3 × 0.3	38 × 5	3 × 3	0.5 × 0.5	Improved entry knowledge with EDL navigation that enables pinpoint landing with minimal maneuvering.

during mission critical events. Indeed, future relay orbiters that will make up the Mars Network, such as the MRO, will have budgeted maneuvering capability to ensure coverage for a Mars mission during critical events [5]. By design, the Electra is also capable of collecting Doppler data concurrent with data transmission while the link is active. Furthermore, the Electra has been designed with spare processing and memory capabilities that can be used for higher-level processing. Given a baseline scenario in which radiometric data between a Mars Network orbiter and an approaching spacecraft are available, the paper describes a technology task that is developing a real-time, embedded Mars approach and EDL navigation filter for the Electra uhf transceiver to achieve 300 m or better atmosphere entry knowledge error, as indicated by the cells containing italics in Table 1. The resulting technology enables pinpoint landings that minimize maneuvering during EDL, as shown in the third row of Table 1. Ultimately, the navigation technology should be integrated with a spacecraft's onboard guidance system for complete closed-loop guidance and navigation (GN). Doing so will achieve a 300 m or better atmosphere delivery error. However, the paper addresses only the navigation portion of the complete GN system.

II. Concept of Operations

The Mars Network, which consists of science orbiters whose secondary mission is to serve as telecommunications relays, will provide proximity telecommunications for increased science data return, critical event real-time telemetry capture, and navigation and timing services for in situ navigation and surface positioning. Currently, the network consists of the 2001 Mars Odyssey orbiter, which carries the CE-505 radio developed by Cincinnati Electronics, and the 2005 Mars Reconnaissance Orbiter, which carries the Electra radio developed by the Jet Propulsion Laboratory (JPL). Both orbiters contain enough propellant reserves to sustain operation through at least 2015 [6]. It is anticipated that future Mars missions, such as the 2009 Mars Science Laboratory, will carry some variant of the Electra radio, except for the 2007 Phoenix Mars lander, which for heritage reasons will carry the CE-505 radio.

The Electra is a programmable, software-defined uhf radio that can be driven by an external oscillator, which for the MRO is an ultrastable oscillator (USO). The programmability extends from tracking loop design to onboard real-time measurement processing, making the device extremely flexible in its range of operation. The current Electra design features a space-qualified SPARC V-7 processor running at 24 MHz with 256 Mbits of storage and between 1 MB [electrically erasable programmable read only memory (EEPROM)] and 2 MB [static random access memory (SRAM)] of executable memory. It is estimated that about two-thirds of the processing and memory is available for use. The Electra radiates a biphase shift keying (BPSK) signal at varying output levels typically less than 10 W as required for a particular mission. The signal can be transmitted in one of three modes: carrier only, BPSK with residual carrier, and BPSK with suppressed carrier. Several forward error corrections schemes are available for use, including Manchester decoding for residual carrier operation and 3-bit soft decision Viterbi decoding for suppressed carrier operation. Data rates from 1 to 2048 ksps are available.

Electra can provide spacecraft-to-spacecraft radiometric navigation data between a Mars Network orbiter and any other spacecraft by measuring the carrier phase of the Doppler shifted signal. The raw navigation measurement of the Electra transceiver is either one-way total count phase $O^{1\mathrm{WTP}}$ or two-way total count phase $O^{2\mathrm{WTP}}$ of the received carrier. Conceptually, the two-way total count phase measurement is:

$$O^{2\mathrm{WTP}}(t) = \phi^{\mathrm{tr}}[t - \rho(t) - \delta_{2W}] - \phi^{\mathrm{tr}}(t) - N \tag{1}$$

where $\phi^{\mathrm{tr}}(t)$ is the phase of the transceiver's oscillator at the specified time, $\rho(t)$ is the round-trip light time, δ_{2W} is any additional hardware delay in the two-way transmission path, and N is the unknown phase ambiguity. A detailed model of the two-way total count phase measurement is provided in Sec. IV. To remove the unknown phase ambiguity, the one-way and two-way total count phase measurements are usually processed as integrated Doppler measurements that are the difference of two phase measurements separated by a specified count time T. For accurate integrated Doppler measurements, continuous tracking without cycle slips is required throughout the count time. It is the integrated Doppler observable that will ultimately be used in the navigation filter. The two-way integrated Doppler observable $O^{2\mathrm{WID}}$ is related to the two-way total count phase $O^{2\mathrm{WTP}}$ according to

$$O^{2\mathrm{WID}}(t) = -[O^{2\mathrm{WTP}}(t) - O^{2\mathrm{WTP}}(t-T)] \tag{2}$$

The Electra can operate in both a one-way and a two-way tracking mode. In the two-way tracking mode, a transceiver onboard an approaching spacecraft transmits a signal at 401 MHz to a transponder onboard a Mars Network orbiter that phase-coherently retransmits the signal at 437 MHz back to the approaching spacecraft, which then records the measurement. The advantage of the two-way measurement is that it eliminates the error contribution from the transponder's oscillator. The one-way measurement, on the other hand, includes error contributions from two independent oscillators: one on the transmitter and the other on the receiver. Full duplex communications with coherent two-way data are currently supported only when the Electra transceiver is on a Mars Network orbiter and the transponder is on an approaching spacecraft or surface lander. The Electra is capable of swapping transmit and receive bands, but is only able to do so in half-duplex mode, which does not support coherent turnaround [7]. This is primarily a software issue, and it is anticipated that the capabilities of the Electra will be

Table 2 Nominal orbital elements of the MRO and the MSL in Mars-centered inertial coordinates

Orbital element	MRO	MSL
Semimajor axis, km	3684.5	−5432.0
Eccentricity	0.010	1.617
Inclination, deg	93.0	44.1
Longitude of node, deg	278.0	91.9
Argument of periapsis, deg	270.0	297.2

Table 3 MSL entry state[a] in Mars-centered inertial coordinates

State–vector component	Value
X	2509.459003 km
Y	377.697451 km
Z	−2442.509568 km
$\dot{X}$	−1.473129134 km/s
$\dot{Y}$	5.335713468 km/s
$\dot{Z}$	1.264687130 km/s

[a]Entry defined at an altitude of 125 km above the surface of Mars.

extended to support two-way Doppler measurements in either direction shortly.

III. Scenario Definition

The performance analysis used in the study is based on the 2010 encounter at Mars between the MRO and the MSL spacecraft. The MRO spacecraft, which will function as the Mars Network orbiter in the analysis, entered its primary science orbit in 2006. The orbit is a 255 × 320 km near-polar orbit with periapsis frozen over the South Pole. The orbit is sun synchronous with an ascending node orientation that provides a local mean solar time of 1500 hrs at the equator [8]. The nominal orbital elements of the MRO mission are summarized in Table 2.

The MSL mission, which will serve as the approaching spacecraft in the analysis, is currently scheduled to launch in 2009 with arrival at Mars in the fall of 2010. Although the landing site has not been selected, analysis of cruise, final approach, and EDL has been performed by the project for various combinations of launch date, arrival date, and landing site. The baseline approach trajectory used in the analysis is based on one of these cases studied by the MSL project and is given in Table 2. The atmospheric entry state for the selected MSL trajectory, which is listed in Table 3, corresponds to the final condition of the valid Earth–Mars transfer trajectory that was used for approach navigation analysis [9]. When combined with an assumed entry body and EDL time line, the entry state is also the initial condition for a trajectory that lands at the desired landing site, defined for the analysis as 41.45°S latitude and 286.74°E longitude. The details of the trajectory are not as important to the analysis as the fact that they represent a reasonable final approach and EDL trajectory for the MSL and a reasonable trajectory for a pinpoint landing scenario from entry to parachute deploy or to the end of the entry guidance phase. Although the MSL will not be attempting a pinpoint landing as defined previously, the hypersonic guidance strategy assumed in the analysis is a viable candidate for future pinpoint landing missions [10,11]. Other entry guidance options that are under consideration for pinpoint landing, including hypersonic guidance approaches not derived from the Apollo Earth-return guidance and approaches optimized for higher L/D entry bodies, should all benefit from improved onboard state knowledge.

A. Dynamic Analysis

The performance of any navigation filter will depend on the performance of the carrier tracking loops and their ability to acquire and track the signal throughout the final approach and EDL phases. The regions of particular interest include 1) the maximum distance at which the link can be closed, 2) the region of greatest relative velocity when the Doppler shift is a maximum, and 3) the region of greatest relative acceleration when the change in Doppler shift is a maximum. The standard approach scenario during the 2010 encounter at Mars between the MRO and the MSL spacecraft is used to determine these regions and set bounds on the expected Doppler shifts.

The dynamic analysis is dependent on several assumptions regarding the attitudes of the MSL and the MRO spacecraft, including the types of antennas used and their locations on the spacecraft. The MSL spacecraft is assumed to spin at a rate of 2 rpm about the $+z$ axis of the spacecraft body-fixed frame. The attitude of the MSL spacecraft is constrained by the X-band link between the cruise medium-gain antenna (CMGA) and the Deep Space Network (DSN), which requires that the Earth lie within 5 deg of the $-z$ axis, as shown in Fig. 2. The MSL spacecraft is assumed to have three uhf patch antennas, which are located on the lower cone of the backshell and are separated by 120 deg. The lower cone of the backshell is inclined 50 deg to the $-z$ axis of the body frame. (In the current MSL design, the three uhf patch antennas have been replaced by a single wrap-around antenna. However, the results of the analysis are still valid.)

As for the MRO spacecraft, current operations requirements indicate that it will be able to track an approaching spacecraft for upwards of 30 min in a given orbit before it will need to off point for battery reasons. All of the approach simulations assume this strategy and include only 30-min tracks, which amounts to about six tracking passes during the final approach phase, as will be shown shortly. Note that the last pass is designed to cover the final 30 min of the approach and EDL, down to the landing.

The inertial velocity and acceleration of the patch antennas on the MSL spacecraft are given by

$$\dot{\mathbf{r}}^{I}_{\text{antenna}} = \dot{\mathbf{r}}^{I}_{\text{MSL}} + \boldsymbol{\omega}^{I}_{\text{MSL}} \times \mathbf{r}^{B}_{\text{antenna}} \tag{3}$$

$$\ddot{\mathbf{r}}^{I}_{\text{antenna}} = \ddot{\mathbf{r}}^{I}_{\text{MSL}} + \boldsymbol{\omega}^{I}_{\text{MSL}} \times \left(\boldsymbol{\omega}^{I}_{\text{MSL}} \times \mathbf{r}^{B}_{\text{antenna}}\right) \tag{4}$$

where $\mathbf{r}^{B}_{\text{antenna}}$ is the position of the patch antenna with respect to the body-fixed frame, $\boldsymbol{\omega}^{I}_{\text{MSL}}$ is the angular velocity of the MSL, and $\dot{\mathbf{r}}^{I}_{\text{MSL}}$ and $\ddot{\mathbf{r}}^{I}_{\text{MSL}}$ are the inertial velocity and acceleration of the center of mass of the MSL, respectively. The range, range rate, and range acceleration between the MSL and the MRO are given by

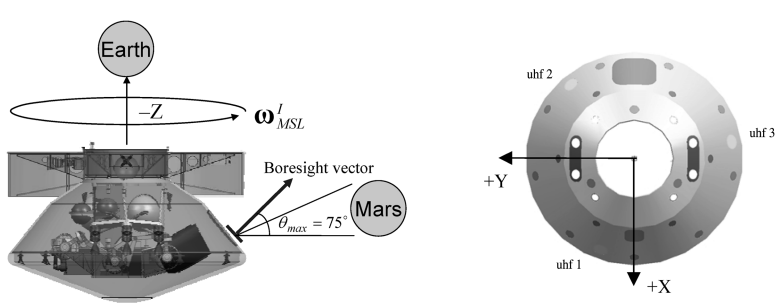

a) Antenna pointing geometry **b) Backshell location of uhf antennas**

Fig. 2 MSL antenna locations and pointing directions.

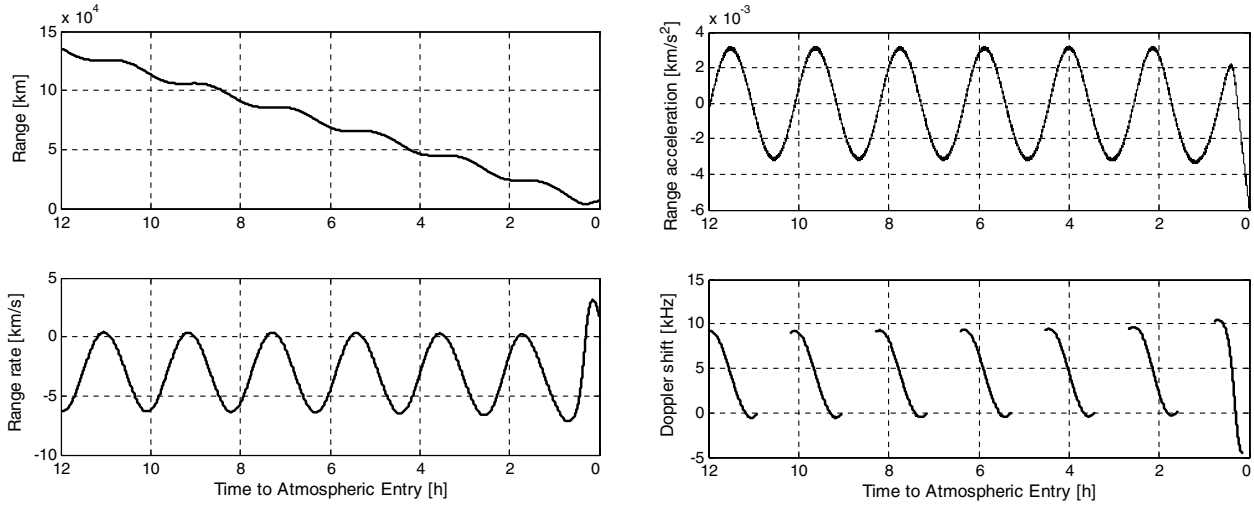

Fig. 3 Range, range rate, range acceleration, and Doppler shift with occultation during the final approach.

$$r = \left|\mathbf{r}^I_{\mathrm{MSL}} + \mathbf{r}^B_{\mathrm{antenna}} - \mathbf{r}^I_{\mathrm{MRO}}\right| \tag{5}$$

$$\dot{r} = \left(\dot{\mathbf{r}}^I_{\mathrm{antenna}} - \dot{\mathbf{r}}^I_{\mathrm{MRO}}\right)^T \hat{\mathbf{e}}^I_r \tag{6}$$

$$\ddot{r} = \left(\ddot{\mathbf{r}}^I_{\mathrm{antenna}} - \ddot{\mathbf{r}}^I_{\mathrm{MRO}}\right)^T \hat{\mathbf{e}}^I_r \tag{7}$$

where $\mathbf{r}^I_{\mathrm{MSL}}$ and $\mathbf{r}^I_{\mathrm{MRO}}$ are the inertial positions of the center of masses of the MSL and the MRO, respectively, $\dot{\mathbf{r}}^I_{\mathrm{MRO}}$ and $\ddot{\mathbf{r}}^I_{\mathrm{MRO}}$ are the inertial velocity and acceleration of the center of mass of the MRO, respectively, and $\hat{\mathbf{e}}^I_r$ is a unit vector from the MRO to the MSL. Note that the motion of the MRO antenna relative to the center of mass is neglected in the dynamic analysis because the MRO antenna is assumed to continually track the approaching spacecraft.

Finally, the Doppler shift is given by

$$\Delta f = f_R - f_T = -\frac{f_T \dot{r}}{c} \tag{8}$$

where f_R and f_T are the received and transmitted signal frequencies, respectively, and c is the speed of light. The results of the dynamic analysis are shown in Fig. 3, which shows the range, range rate, range acceleration, and Doppler shift between the MRO and the MSL during the final approach phase. The results show that the Doppler shift peaks regularly at approximately 9.5 kHz throughout the majority of the approach, although just before atmospheric entry, the Doppler shift reaches its maximum value of 10.5 kHz. The oscillations in the Doppler shift are the result of the periodic orbit of the MRO, which also causes the six periods of signal outage that are the result of the occultation of the line-of-sight vector between the MRO and the MSL because of the presence of Mars between the two spacecraft. The range acceleration oscillates in a similar manner between approximately -3 to 3 $\mathrm{m/s^2}$ throughout most of the final approach and increases to about -6 $\mathrm{m/s^2}$ just before atmospheric entry.

B. Link Analysis

The complete two-way link budget used in the analysis begins with the output of the transceiver aboard the MSL and follows the link path to the transponder on the MRO, in which the signal is retransmitted back to the MSL. A single transmit–receive leg of the link is analyzed in detail with the understanding that except for the transmit frequency (401 vs 437 MHz) and the reversal of the antenna gains, the second half of the link is approximately the same.

The total received power in decibel milliwatts (dBm) is given by [12]

$$P_{rt} = 10\log(P_{\mathrm{watts}}) + G_t + L_i + L_s + L_p + G_r + L_r + 30 \tag{9}$$

where P_{watts} is the transmitted power in watts, G_t is the net transmitter gain, L_i is the transmitter line losses, L_s is the space loss, L_p is the polarization loss, G_r is the net receiver gain, L_r is the receiver line losses, and 30 dB is a product of the conversion from watts to milliwatts. The total received power depends strongly on the antenna radiation patterns. As shown in Fig. 2b, the MSL is assumed to have three uhf patch antennas. The patch antennas are right-hand circularly polarized (RHCP) with a greater than 6 $\mathrm{dB_{ic}}$ gain at the boresight. Note that the subscript ic indicates that the gain is referenced to a circularly polarized radiator. The polarization is elliptical, however, with a maximum axial ratio of -5 dB. Consequently, the alignment and rotation of the patch antennas with respect to the incoming signal can be such that the maximum effective boresight gain is 1 $\mathrm{dB_{ic}}$. Figure 4 shows the assumed model of the antenna radiation patterns in 1) the horizontal plane and 2) the vertical plane. Note that only the main lobe is included in the model; the side lobes have been neglected. Since the actual alignment and rotation of the patch antennas are unknown, the worst-case scenario is assumed in the analysis. Consequently, the maximum gain at boresight is assumed to be 1 $\mathrm{dB_{ic}}$. Furthermore, the half-power beamwidth is assumed to be 80 deg and the gain at 90 deg is assumed to be -5 $\mathrm{dB_{ic}}$. Finally, the voltage standing wave ratio at the frequencies of operation is 2:1. Note that the radiation patterns shown in Fig. 4 are not based on actual measurements. Instead, they are models that have been derived from the assumptions stated previously.

The net receiver gain depends on the off-boresight angle and is calculated using the radiation patterns shown in Fig. 4. The off-boresight angle, which is the angle between the antenna boresight vector and the direction of the incoming Electra signal, is determined by the attitude of the MSL spacecraft during approach and the locations of the uhf patch antennas on the backshell. Analysis has revealed that the off-boresight angle varies between 30–60 deg during the majority of the approach but increases to 50–70 deg during the last part of the approach. Consequently, the Electra signal is received at approximately or slightly outside of the half-power beamwidth.

The total received power at each antenna is determined by the off-boresight angles. As the spacecraft rotates and the total received power at each antenna varies, a switching algorithm compares the power at each antenna and selects the antenna that is receiving the most power. The total received power during the final approach is shown in Fig. 5a. Note that the analysis includes the effect of occultation and of the MSL spin rate, which results in a 2–3 dBm variation in the total received power as the patch antennas pass in and out of the Electra signal. The total received power required by the Electra to close the link has been determined by hardware tests in the laboratory to be -150 dBm. The figure shows that link closure can be maintained continuously from about 10 h before atmospheric entry, giving a total of six tracking passes. Note that 10 h before

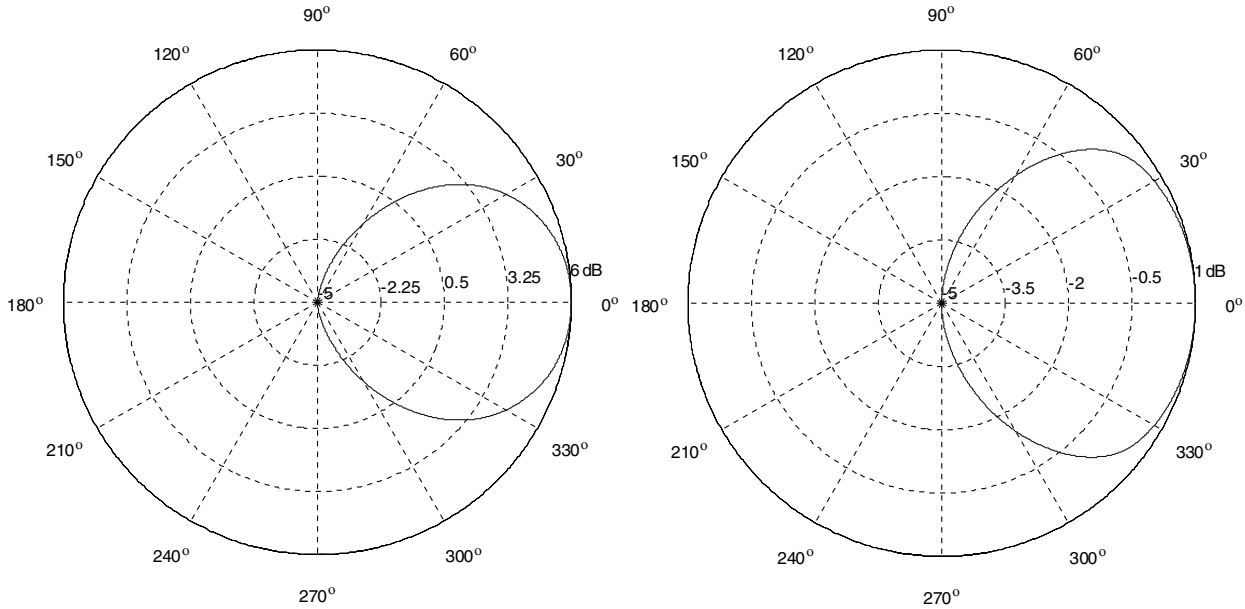

a) Horizontal plane **b) Vertical plane**

Fig. 4 Antenna radiation patterns in two orthogonal planes. Only the main lobe is modeled.

atmospheric entry corresponds to a range of about 110,000 km, as shown in Fig. 3. The values of the link budget parameters that were assumed in the calculation of total received power are given in Table 4.

The bit energy-to-noise density ratio is given by

$$\frac{E_b}{N_0} = \frac{C}{N_0} - 10 \log B_R \tag{10}$$

where C is the carrier power, N_0 is the noise density, and B_R is the bit rate in symbols per second. Note that the carrier power-to-noise density ratio C/N_0 is equal to the total received power-to-noise density ratio P_{rt}/N_0; thus, if the noise density is known, the bit energy-to-noise density can be calculated according to Eq. (10).

The signal-to-noise ratio (SNR) of a phase-modulated signal is given by

$$\mathrm{SNR} = \frac{B_R}{B_W}\frac{E_b}{N_0} \tag{11}$$

where B_W is the filter bandwidth. For a BPSK modulation scheme, the quantity B_R/B_W is taken to be 1. Hence, the SNR is ideally equal to E_b/N_0. However, there is significant signal power loss through the complex baseband process in the Electra, and fixed-point simulations have revealed that for data rates between 8 and 1024 ksps, the SNR is given by [13]

$$\mathrm{SNR} = 0.62\frac{E_b}{N_0} \tag{12}$$

Table 4 Link budget parameters

Parameter	Value
Transmit power	8.5 W
Transmit frequency	437 MHz
Symbol rate	1 ksps
System noise temperature	526 K
Net transmitter antenna gain	3.5 dB
Transmitter line loss	−2 dB
Polarization loss	−1 dB
Receiver line loss	−2 dB

The SNR for data rates between 1 and 1024 ksps are shown in Fig. 5b. The SNR depends strongly on the data rate and varies between −40 and +20 dB throughout the final approach. Note that the Electra signal can also be transmitted in a carrier-only mode, without data modulation, to aid acquisition of the signal during the initial phase of the final approach.

The link analysis has demonstrated the availability of a uhf link from about 10 h before atmospheric entry based on range, geometry, and antenna patterns only. However, environmental effects reduce the availability of the link during EDL. Of particular interest to the EDL problem is plasma blackout caused by increased electron content around the entry body because of the extreme heating during hypersonic flight. Unfortunately, plasma outages are inversely proportional to the transmission band, resulting in significant outages for uhf-band transmissions that are the focus of the analysis. A sample analysis performed for the 2007 Phoenix Mars lander project has been obtained and used to approximate the link outages expected during EDL. Figure 6 shows the results of that analysis for several transmitter bands including uhf. The main difference between the Phoenix mission and the MSL mission is the angle of attack of the entry body. The MSL achieves lift by creating a center of mass offset relative to the center line of the entry body, as opposed to using an aerodynamic shape. For this configuration, the resulting angle of attack for the full lift-up configuration, defined as zero bank angle, results in a decrease of the electron distribution above the local horizontal and an increase in the electron distribution below the local horizontal. The electron distribution is assumed to remain fixed relative to the bank angle. In other words, for a 90-deg positive bank, the electron distribution relative to the zero-lift case will be lower in the direction of lift and higher opposite the lift direction. For the purposes of applying the results of the plasma study to the navigation analysis, assumptions on the orientation of the signal path relative to the entry body are required. A worst-case assumption of 110 s as the start of the plasma outage is used for the study with no additional Doppler data collection after the start of the plasma outage.

IV. Spacecraft-to-Spacecraft Navigation Algorithms

To achieve the goal of having a navigation filter running on the Electra processor, the algorithms required must be defined. The

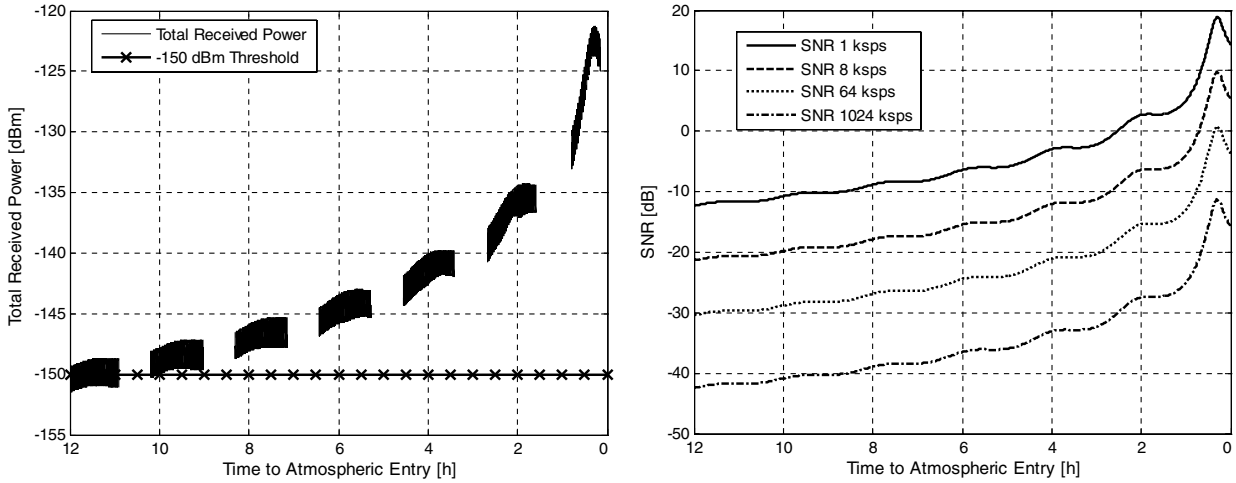

a) Total received power **b) SNR**

Fig. 5 Total received power and SNR during final approach.

selection of algorithms is separated into three main areas. The first area is dynamic modeling, which includes all the forces and moments acting on the spacecraft. The second area is measurement modeling, which includes all incoming data that are to be processed with the filter. The third area is the selection of a filter algorithm. Each of these areas is covered in detail.

A. Dynamic Models

There are several options for the level of fidelity in the dynamics model. It is possible simply to integrate the inertial measurement unit (IMU) output and only model the gravitational acceleration, but here it is assumed that the accelerometer output is processed as a measurement to update the spacecraft's position and velocity whereas the gyro output is integrated directly to propagate the attitude.

The filter dynamics model is based on a development of an EDL reconstruction tool for the MER mission [14], which was subsequently used for an aerobraking analysis tool developed for the MRO mission [15]. The models are used to propagate the spacecraft state and uncertainties in time.

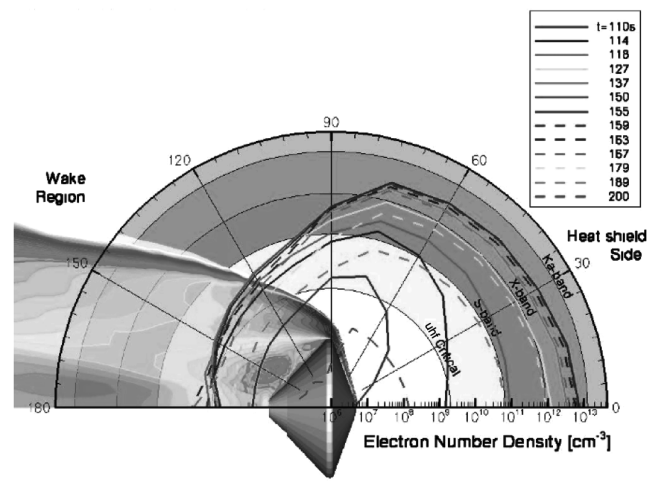

Fig. 6 Electron density from plasma resulting from aerodynamic heating for an entry vehicle. For a backshell-mounted antenna and an arbitrary signal path, the outage starts before 110 s from entry interface and is shown to end before 200 s from entry.

The state vector at time t_k for the MSL is defined by

$$\mathbf{X}_{k_{(9\times1)}} = \begin{bmatrix} \mathbf{r}^I_{\text{cg}} & (3\times1) \\ \mathbf{v}^I_{\text{cg}} & (3\times1) \\ \delta\mathbf{a}^B_{\text{cg,unmod}} & (3\times1) \end{bmatrix} = \begin{bmatrix} \text{vehicle cg position, planet-centered inertial frame} \\ \text{vehicle cg velocity, planet-centered inertial frame} \\ \text{vehicle cg unmodeled accelerations, vehicle cg, origin body frame} \end{bmatrix} \tag{13}$$

(A similar-state vector is defined for the MRO in the navigation filter.) Applying the dynamics modeling assumptions stated here, the equations of motion $\mathbf{F}_k$ for the state vector $\mathbf{X}_k$ are

$$\mathbf{F}_k = \dot{\mathbf{X}}_{k_{(9\times1)}} = \begin{bmatrix} \dot{\mathbf{r}}^I_{\text{cg}} & (3\times1) \\ \dot{\mathbf{v}}^I_{\text{cg}} & (3\times1) \\ \delta\dot{\mathbf{a}}^B_{\text{cg,unmod}} & (3\times1) \end{bmatrix} = \begin{bmatrix} \mathbf{v}^I_{\text{cg}} \\ \frac{1}{M_{\text{SC}}}\mathbf{F}^I_{\text{ng,dyn}} + \mathbf{T}^I_B\delta\mathbf{a}^B_{\text{cg,unmod}} + \mathbf{g}^I_{\text{cg}} \\ -\mathbf{B}_a\delta\mathbf{a}^B_{\text{cg,unmod}} \end{bmatrix} \tag{14}$$

where $\mathbf{B}_a$ defines the acceleration noise propagation, given by

$$\mathbf{B}_a = \begin{bmatrix} 1/\tau_{a_x} & 0 & 0 \\ 0 & 1/\tau_{a_y} & 0 \\ 0 & 0 & 1/\tau_{a_z} \end{bmatrix} \tag{15}$$

Note that the acceleration time constants τ_a in Eq. (15) are determined from the IMU noise model.

To perform time updates on the covariance matrix, a state transition matrix $\mathbf{\Phi}_{kk}(t_i, t_{i-1})$ is required. For the state vector $\mathbf{X}_k$ defined here, the state transition matrix is

$$\mathbf{\Phi}_{kk}(t_i, t_{i-1}) = \begin{bmatrix} \phi_{rr_{(3\times3)}} & \phi_{rv_{(3\times3)}} & \phi_{ra_{(3\times3)}} \\ \phi_{vr_{(3\times3)}} & \phi_{vv_{(3\times3)}} & \phi_{va_{(3\times3)}} \\ \phi_{ar_{(3\times3)}} & \phi_{av_{(3\times3)}} & \phi_{aa_{(3\times3)}} \end{bmatrix} = \begin{bmatrix} \mathbf{I}_{(3\times3)} & \phi_{rv_{(3\times3)}} & \phi_{ra_{(3\times3)}} \\ \mathbf{0}_{(3\times3)} & \mathbf{I}_{(3\times3)} & \phi_{va_{(3\times3)}} \\ \mathbf{0}_{(3\times3)} & \mathbf{0}_{(3\times3)} & \mathbf{I}_{(3\times3)} \end{bmatrix} \tag{16}$$

where

$$\phi_{rv_{(3\times3)}} = \frac{\partial \mathbf{r}^I_{\mathrm{cg}}(t_i)}{\partial \mathbf{v}^I_{\mathrm{cg}}(t_{i-1})} = \mathbf{I}_{(3\times3)}\Delta t$$
$$\phi_{ra_{(3\times3)}} = \frac{\partial \mathbf{r}^I_{\mathrm{cg}}(t_i)}{\partial \delta\mathbf{a}^B_{\mathrm{cg,unmod}}(t_{i-1})} = \mathbf{T}^I_{B_{(3\times3)}}\frac{\Delta t^2}{2} \tag{17}$$
$$\phi_{va_{(3\times3)}} = \frac{\partial \mathbf{v}^I_{\mathrm{cg}}(t_i)}{\partial \delta\mathbf{a}^B_{\mathrm{cg,unmod}}(t_{i-1})} = \mathbf{T}^I_{B_{(3\times3)}}\Delta t$$

Note that the time interval Δt in Eq. (17) is assumed to be small for the equations to be valid.

B. Measurement Models

1. IMU Measurements

The IMU data include output from three orthogonal gyros and three orthogonal accelerometers for the approaching spacecraft. The models here are based on the current data processing strategy, which is still under development. The strategy is to process the IMU output via filtering of the accelerometer measurements to update the position and velocity and to directly integrate the gyro measurements to update the attitude.

The model used to create the gyro measurements from the true body angular rates is

$$\boldsymbol{\omega}_{G_{(3\times1)}} = \mathbf{M}_{\mathrm{SF}_{G_{(3\times3)}}}[\mathbf{I}_{(3\times3)} + \mathbf{M}_{\mathrm{MA}_{G_{(3\times3)}}} + \mathbf{M}_{\mathrm{NO}_{G_{(3\times3)}}}]\mathbf{T}^G_{B_{(3\times3)}}\boldsymbol{\omega}^B_{\mathrm{SC}_{(3\times1)}} + \mathbf{b}_{G_{(3\times1)}} + \boldsymbol{\varepsilon}_{G_{(3\times1)}} \tag{18}$$

To define the accelerometer measurement, a brief description of the problem is required. An accelerometer can only sense nonconservative forces and requires outside models for conservative forces to define the total acceleration. For this problem, the only conservative force is gravity. At a minimum, a gravity model is required to directly integrate the data to correctly propagate the trajectory. Since the setup involves filtering the accelerometer data, additional models are required to allow the filter to apply corrections to specific physical models and the remaining unmodeled acceleration parameters. The model used to create the accelerometer measurements from the nongravitational acceleration is

$$\mathbf{a}_{A_{(3\times1)}} = \mathbf{M}_{\mathrm{SF}_{A_{(3\times3)}}}[\mathbf{I}_{(3\times3)} + \mathbf{M}_{\mathrm{MA}_{A_{(3\times3)}}} + \mathbf{M}_{\mathrm{NO}_{A_{(3\times3)}}}]\mathbf{T}^A_{B_{(3\times3)}}\mathbf{a}^B_{A_{(3\times1)}} + \mathbf{b}_{A_{(3\times1)}} + \boldsymbol{\varepsilon}_{A_{(3\times1)}} \tag{19}$$

where $\mathbf{a}^B_A$ is

$$\mathbf{a}^B_{A_{(3\times1)}} = \mathbf{T}^B_{I_{(3\times3)}}\mathbf{a}^I_{\mathrm{cg,ng,mod}_{(3\times1)}} + \delta\mathbf{a}^B_{\mathrm{cg,unmod}_{(3\times1)}} + \boldsymbol{\omega}^B_{\mathrm{SC}(3\times1)} \times \boldsymbol{\omega}^B_{\mathrm{SC}(3\times1)} \times \mathbf{r}^B_{A/\mathrm{cg}_{(3\times1)}} + [\boldsymbol{\alpha}^B_{\mathrm{SC,mod}_{(3\times1)}} + \boldsymbol{\alpha}^B_{\mathrm{SC,unmod}_{(3\times1)}}] \times \mathbf{r}^B_{A/\mathrm{cg}_{(3\times1)}} \tag{20}$$

The measurement partials used to process the accelerometer measurements $\mathbf{H}_A$ are a simplified version of the model used to simulate the measurements. First, the accelerometer reports unbiased nongravitational forces, so that $\mathbf{b}_A = 0$. In addition, the scale factor error, misalignment error, and nonorthogonality error are all zero. Hence $\mathbf{M}_{\mathrm{SF}_A}$ is the identity matrix, whereas $\mathbf{M}_{\mathrm{MA}_A}$ and $\mathbf{M}_{\mathrm{NO}_A}$ are zero matrices. With these assumptions, the accelerometer measurement partials are given by

$$\mathbf{H}_{A_{(3\times9)}} = \frac{\partial \mathbf{T}^A_B\mathbf{a}^B_A}{\partial \mathbf{X}_k} = \mathbf{T}^A_B\frac{\partial \mathbf{a}^B_A}{\partial \mathbf{X}_k} = \mathbf{T}^A_B\left[\frac{\partial \mathbf{a}^B_A}{\partial \mathbf{r}^I_{\mathrm{cg}_{(3\times1)}}}\middle|\frac{\partial \mathbf{a}^B_A}{\partial \mathbf{v}^I_{\mathrm{cg}_{(3\times1)}}}\middle|\frac{\partial \mathbf{a}^B_A}{\partial \delta\mathbf{a}^B_{\mathrm{cg,unmod}_{(3\times1)}}}\right] \tag{21}$$

where

$$\frac{\partial \mathbf{a}^B_A}{\partial \mathbf{r}^I_{\mathrm{cg}_{(3\times3)}}} = \mathbf{T}^B_I\frac{1}{M_{\mathrm{SC}}}\frac{\partial \mathbf{F}^I_{\mathrm{ng,dyn}}}{\partial \mathbf{r}^I_{\mathrm{cg}}} + \mathbf{R}_{A/\mathrm{cg}_{(3\times3)}}\mathbf{J}^{-1}_{\mathrm{SC}}\mathbf{T}^B_I\frac{\partial \boldsymbol{\tau}^I_{\mathrm{dyn}}}{\partial \mathbf{r}^I_{\mathrm{cg}}}$$
$$\frac{\partial \mathbf{a}^B_A}{\partial \mathbf{v}^I_{\mathrm{cg}_{(3\times3)}}} = \mathbf{T}^B_I\frac{1}{M_{\mathrm{SC}}}\frac{\partial \mathbf{F}^I_{\mathrm{ng,dyn}}}{\partial \mathbf{v}^I_{\mathrm{cg}}} + \mathbf{R}_{A/\mathrm{cg}_{(3\times3)}}\mathbf{J}^{-1}_{\mathrm{SC}}\mathbf{T}^B_I\frac{\partial \tau^I_{\mathrm{dyn}}}{\partial \mathbf{v}^I_{\mathrm{cg}}} \tag{22}$$
$$\frac{\partial \mathbf{a}^B_A}{\partial \delta\mathbf{a}^B_{\mathrm{cg,unmod}_{(3\times3)}}} = \mathbf{I}_{(3\times3)}$$

and where the 3×3 matrix $\mathbf{R}_{A/\mathrm{cg}}$ is an expansion of the cross-product operator

$$\mathbf{R}_{A/\mathrm{cg}} = \times\mathbf{r}^B_{A/\mathrm{cg}} = \begin{bmatrix} 0 & z^B_{A/\mathrm{cg}} & y^B_{A/\mathrm{cg}} \\ -z^B_{A/\mathrm{cg}} & 0 & x^B_{A/\mathrm{cg}} \\ y^B_{A/\mathrm{cg}} & -x^B_{A/\mathrm{cg}} & 0 \end{bmatrix} \tag{23}$$

2. Electra Measurements

A key radiometric observable that the Electra transceiver will formulate is a two-way total count carrier phase $O^{2\mathrm{WTP}}$ at the uhf band. The $O^{2\mathrm{WTP}}$ observable contains information that can be related to the two-way integrated Doppler observable $O^{2\mathrm{WID}}$ between an Electra transceiving element and a transponding element. The following provides the mathematical basis for formulating these observables using a detailed model of the Electra transceiving and transponding elements and the Electra clock that is used to time tag the measurements.

Electra's signal and clock functions are derived from a common reference oscillator that nominally operates at 76 MHz. Each of the observables $O(\cdot)$ is derived from the reference oscillator with a frequency $f(t)$ and stamped with a time tag from a local clock $\tau(t)$ that is also derived from the oscillator. A sufficient model for the frequency $f(t)$ of the reference oscillator is

$$f(t) = f_0[(1 + d) + a(t - t_0)] + \frac{\mathrm{d}\psi(t)}{\mathrm{d}t} \tag{24}$$

where t is the true time, t_0 is the epoch in true proper time that is associated with the oscillator model parameters, d is the clock drift or oscillator fractional frequency offset, a is the clock acceleration or oscillator aging, $\psi(t)$ is the oscillator random phase process in cycles with $E[\psi(t)] = 0$, and f_0 is the nominal reference oscillator frequency of 76.72322224 MHz. The reference oscillator is used to derive a clock in cycles $c(t)$ or as a time $\tau(t)$, which are modeled as

$$c(t) = b + \frac{1}{4}\int_{t_0}^{t} f(t)\mathrm{d}t = b + \frac{f_0}{4}\left[(1 + d)(t - t_0) + a\frac{(t - t_0)^2}{2} + \frac{\psi(t) - \psi(t_0)}{f_0}\right]$$
$$\tau(t) = t_0 + \frac{4}{f_0}[c(t) - b] \tag{25}$$

where b is the clock bias in cycles. The appearance of the 4 in Eq. (25) for both $c(t)$ and $\tau(t)$ is because the frequency used for the clock is divided down from the reference frequency to yield a nominal clock tick of 52.1355 ns.

The physical path of the signal that is measured by the receiving element of the Electra transceiver at time t^i_e originated from the transceiver's transmitting element a round-trip light-time ago plus some hardware delays. The physical path of the signal through the transceiver, which is denoted by the subscript x, and the transponder, which is denoted by the subscript t, and the associated times are

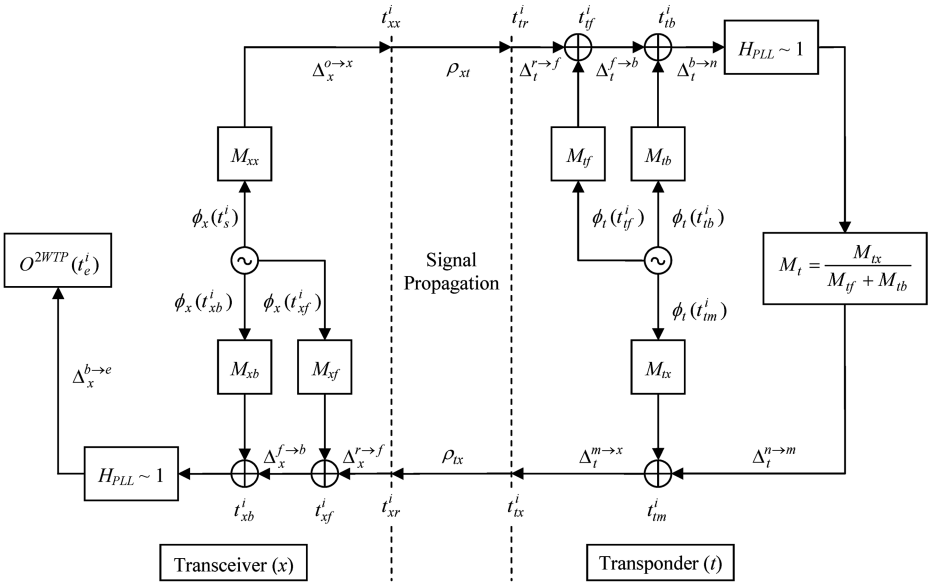

Fig. 7 Block diagram and time line of an Electra two-way total count phase measurement.

illustrated in Fig. 7. The following time and delay definitions apply and are shown in the time sequence illustrated in Fig. 7:

t^i_s = The time that the signal is generated by the transceiver's reference oscillator.

t^i_{xx} = The time that the signal leaves the transceiver antenna. The transceiver transmission delay is defined as $\Delta^{o\to x}_x \equiv t^i_{xx} - t^i_s$ and includes the entire signal transit time from the reference oscillator, through the electronics and antenna line feed, and then exiting the antenna.

t^i_{tr} = The time that the signal is received by the transponder antenna.

t^i_{tf} = The time that the signal is mixed down to the intermediate frequency by the transponder's front-end analog hardware. The delay $\Delta^{r\to f}_t \equiv t^i_{tf} - t^i_{tr}$ is the signal transit time through the antenna line feed to the transponder.

t^i_{tb} = The time that the signal enters the transponder's baseband processing module for bandpass sampling. The delay $\Delta^{f\to b}_t \equiv t^i_{tb} - t^i_{tf}$ is the signal transit time in the analog receiver electronics.

t^i_{tn} = The time that the transponder tracking loop actually measures the phase of the signal. The delay $\Delta^{b\to n}_t \equiv t^i_{tn} - t^i_{tb}$ is the signal transit time through the tracking loops.

t^i_{tm} = The time that the transponder modulates the measured phase back onto the return carrier signal. The delay $\Delta^{n\to m}_t \equiv t^i_{tm} - t^i_{tn}$ is the signal transit time from the tracking loop to remodulation.

t^i_{tx} = The time that the signal leaves the transponder antenna. The delay $\Delta^{m\to x}_t \equiv t^i_{tx} - t^i_{tm}$ is the signal transit time through the transmit electronics and antenna line feed and then exiting the antenna.

t^i_{xr} = The time that the signal is received at the transceiver antenna.

t^i_{xf} = The time that the signal is mixed down to the intermediate frequency by the transceiver's front-end analog hardware. The delay $\Delta^{r\to f}_x \equiv t^i_{xf} - t^i_{xr}$ is the signal transit time through the antenna line feed to the transceiver.

t^i_{xb} = The time that the signal enters the transceiver's baseband processing module for bandpass sampling. The delay $\Delta^{f\to b}_x \equiv t^i_{xb} - t^i_{xf}$ is the transit time in the analog receiver electronics.

t^i_e = The time that the transceiver records the accumulated phase measurement. The delay between bandpass sampling and the measurement is $\Delta^{b\to e}_x \equiv t^i_e - t^i_{xb}$.

ρ_{xt}, ρ_{tx} = One-way light time on the forward link from the transceiver to the transponder and on the return link from the transponder to the transceiver, respectively.

$M_{(*)(*)}$ = Internal fundamental integer multipliers in the transceiver and the transponder, required to achieve the proper frequencies.

Note that there are additional delays that are neither shown in Fig. 7 nor defined here. These include distribution delays from the reference oscillator to the bandpass sampling and intermediate frequency mixing in both the transceiver and the transponder. These additional delays are on the order of a nanosecond or less since the devices are small and the distribution lines are on the order of tens of centimeters or less. Consequently, these additional delays are neglected. Also note that the closed-loop transfer function H_{PLL} (phase-locked loop) for the tracking loop can be approximated with a value of 1 for formulating a low-pass frequency phase model [7].

The two-way total count phase measurement can now be formulated as

$$O^{2\mathrm{WTP}}\left(t^i_e\right) = M_t M_{xx}\phi_x\left(t^i_s\right) - M_{xr}\phi_x\left(t^i_e\right) + \Delta\phi_x\left(\Delta^*_x, t^i_e\right) + \Delta\phi_t\left(\Delta^*_t, t^i_t\right) + \upsilon^{2\mathrm{WTP}}\left(t^i_e\right) \tag{26}$$

where $\Delta\phi_x(\Delta^*_x, t^i_e)$ represents the phase biases, delays, and stochastic errors introduced by the physical time delays in the transceiver and takes the form

$$\Delta\phi_x\left(\Delta^*_x, t^i_e\right) = M_{xr}\phi_x\left(t^i_e\right) - M_{xf}\phi_x\left(t^i_{xf}\right) - M_{xb}\phi_x\left(t^i_{xb}\right) \tag{27}$$

and where $\Delta\phi_t(\Delta^*_t, t^i_t)$ represents the phase biases, delays, and stochastic errors introduced by the physical time delays in the transponder and takes the form

$$\Delta\phi_t\left(\Delta^*_t, t^i_t\right) = M_{tx}\phi_t\left(t^i_{tm}\right) - M_t\left[M_{tf}\phi_t\left(t^i_{tf}\right) - M_{tb}\phi_t\left(t^i_{tb}\right)\right] \tag{28}$$

Note that the aggregate multiplier $M_{xr} = M_{xb} + M_{xf}$ is introduced for simplicity and that the term $\upsilon^{2\mathrm{WTP}}(t^i_e)$ has been included in Eq. (26) to account for noise and errors arising from sources other than the oscillator, such as thermal link noise and multipath. The

fundamental quantity being measured is $M_t M_{xx}\phi_x(t_s^i) - M_{xr}\phi_x(t_e^i)$, which embodies the separate forward- and return-link Doppler shifts as integrated into the carrier phase. Ideally, the phase delays in Eqs. (27) and (28) are small and/or static relative to the fundamental phase shift.

The phase model for the reference oscillator on the transceiver and the transponder is related to the frequency model given in Eq. (24) as follows:

$$\phi_*(t) = \phi_{*0} + \int_{t_0}^{t} f_*(t)\mathrm{d}t = \phi_{*0} + f_{*0}\left[(1+d_*)(t-t_0) + a_*\frac{(t-t_0)^2}{2}\right] + \psi_*(t) - \psi_*(t_0) \tag{29}$$

where the subscript $*$ refers to either the transceiver (x) or the transponder (t). Using the phase model, the two-way total count phase measurement can now be formulated as

$$\begin{aligned} O^{2\mathrm{WTP}}(t_e^i) = {} & -f_{x0}M_tM_{xx}\left[(1+d_x)\Delta_{2W}\left(t_e^i\right) + a_x\Delta_{2W}\left(t_e^i\right)\left(t_e^i - t_0 - \frac{\Delta_{2W}\left(t_e^i\right)}{2}\right)\right] \\ & + f_{x0}(M_tM_{xx} - M_{xr})\left[(1+d_x)\left(t_e^i - t_0\right) + a_x\frac{\left(t_e^i - t_0\right)^2}{2}\right] \\ & + M_tM_{xx}\left[\psi_x\left(t_s^i\right) - \psi_x(t_0)\right] - M_{xr}\left[\psi_x\left(t_e^i\right) - \psi_x(t_0)\right] \\ & + \Delta\phi_x\left(\Delta_x^*, t_e^i\right) + \Delta\phi_t\left(\Delta_t^*, t_t^i\right) + \upsilon^{2\mathrm{WTP}}\left(t_e^i\right) - N \end{aligned} \tag{30}$$

where the total two-way signal delay is defined as

$$\begin{aligned} \Delta_{2W}(t_e^i) &= \Delta_x^{o\to x} + \rho_{xt}\left(t_{tr}^i\right) + \Delta_t^{r\to x} + \rho_{tx}\left(t_{xr}^i\right) + \Delta_x^{r\to e} \\ &= \Delta_x^{o\to x} + \Delta_t^{r\to x} + \Delta_x^{r\to e} + \rho_{xt}\left(t_e^i - \Delta_x^{r\to e} - \rho_{tx}\left(t_e^i - \Delta_x^{r\to e}\right) - \Delta_t^{r\to x}\right) + \rho_{tx}\left(t_e^i - \Delta_x^{r\to e}\right) \end{aligned} \tag{31}$$

The transponder delay is defined as

$$\Delta_t^{r\to x} = \Delta_t^{r\to f} + \Delta_t^{f\to b} + \Delta_t^{b\to n} + \Delta_t^{n\to m} + \Delta_t^{m\to x} \tag{32}$$

and the transceiver receive delay is defined as

$$\Delta_x^{r\to e} = \Delta_x^{r\to f} + \Delta_x^{f\to b} + \Delta_x^{b\to e} \tag{33}$$

It should be noted that the initial phase has been grouped into a term labeled N in Eq. (30) that is typically unknown. The most significant observation regarding Eq. (30) is that the random phase of the transponder oscillator does not appear in the final result. The absence of the random phase contribution is the chief advantage of using two-way over one-way data. To actually use the data for navigation, partial derivatives with respect to dynamic and bias parameters are needed. For the sake of brevity these have not been included in the paper.

The two-way total count phase measurement $O^{2\mathrm{WTP}}(t_e^i)$ is what the Electra physically records. However, it contains unknown phase biases, delays, and stochastic errors. To eliminate these unknowns for navigation, the phase measurements are usually processed as an integrated Doppler measurement that is the difference of two phase measurements separated by a specified count time T. That is, the equation defining the Electra two-way integrated Doppler measurement is given by

$$O^{2\mathrm{WID}}\left(t_e^2, t_e^1\right) = -\left[O^{2\mathrm{WTP}}\left(t_e^2\right) - O^{2\mathrm{WTP}}\left(t_e^1\right)\right] \tag{34}$$

where t_e^1 and t_e^2 are the time tags of the first and second phase measurements and $T \approx t_e^2 - t_e^1$, which is approximate because the Electra clock will drift from the ideal count time T as the real clock progresses from t_e^1 to t_e^2. It is for this reason that the observable is not divided by the measured count time, as doing so would unnecessarily complicate the partials for the observable. So the measurement assumption is that the clock does not drift over the count time T; the real drift is accepted as measurement error.

C. Filter Algorithm

Two different but related filtering approaches were considered. The first is an extended Kalman filter (EKF) [16], considered to be the baseline for any real-time sequential estimation task with nonlinear plant. Several factorization approaches were considered, including a simple Joseph suboptimal covariance update, a square-root implementation based on the work of Carlson [17], and a upper-triangular, diagonal, upper-triangular (UDU) factorized approach based on Bierman [18]. The second approach is a sigma-point filter [19]. The main advantage of the sigma-point filter over an EKF is the lack of a linearization step in computing the propagated covariance. In an EKF, a linearized transition matrix, or other equation based on the first derivative of the dynamics with respect to the state vector, is required to propagate the state covariance in time. This not only introduces linearization errors but also requires the derivation and coding of a series of dynamic partials, which is complex and error prone at best and may not be possible for some highly nonlinear problems. The sigma-point filter avoids the linearization by propagating a small dispersed set of states to the desired time step (the sigma points) and constructs the covariance matrix based on statistics.

Another factor in the filter algorithm selection, and the main criterion used, is the array of operational scenarios envisioned for the filter. To improve the overall return to the advanced EDL work area of their investment, the managers from three of the work area elements agreed to share development costs of the filter. Each element involved navigation using the Electra as a platform and real-time processing. The three applications for the filter being considered include the use of uhf Doppler navigation during final approach, the use of uhf Doppler navigation during EDL, and the use of the Electra as a platform for adaptive estimation during EDL [20]. Although each application has a different solution to optimize the usage of the limited processing resources available on the Electra hardware, a single filter that can be applied to all three problems was desired. For example, a factorized approach is desired for the approach problem but not required for the EDL problem. However, the impact of using a slightly less optimal solution for one particular problem is more than offset by the savings in effort to build and validate a single filter on the hardware as opposed to three separate filters. For the EDL navigation task, an EKF was judged the best option. The equations of motion for the Doppler-based filters are well understood by the team and are highly accurate. The impact of the decision will be discussed later.

With the selection of the EKF for the approach and EDL tasks, the question remains as to which formulation to choose. The EDL problem has the best observability because of the high dynamics but is much more constrained by processing time constraints than the approach problem. In contrast, the approach problem is much more numerically problematic, requiring factorization beyond the optimal EKF formulation and the Joseph update form. Based on the experience of the team and the external resources available for the development, the Bierman UDU factorization was selected. While providing the numerical stability required for the approach problem with its large variation in signal path distance, the approach does not impose additional computational burden above the standard EKF [18].

V. Navigation Performance

High-fidelity simulations of the final approach were run to determine the navigation performance for three different tracking scenarios, as described in the following section. A separate covariance analysis was also performed to determine the navigation performance during EDL.

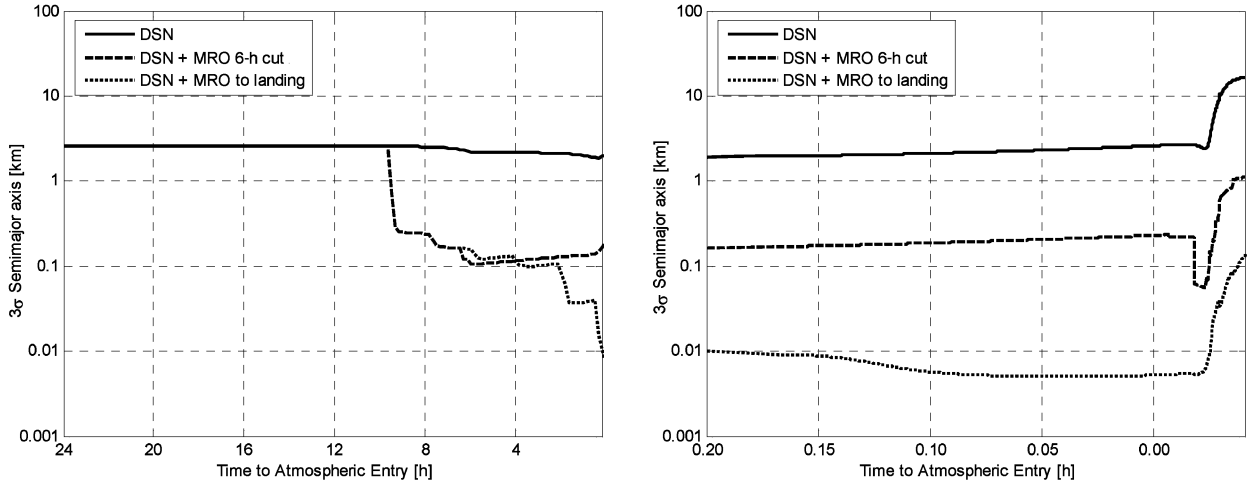

a) b)

Fig. 8 Semimajor axis knowledge produced by a Mars Network orbiter tracking a Mars approach vehicle, showing a) the final day before entry and b) the time from separation to landing.

A. Approach Navigation Performance

The results of a simulation of the MSL approach trajectory are shown in Fig. 8, which depicts the 3σ semimajor axis of the current state position uncertainty in the final day before entry and from separation to landing. Note that EDL begins at atmospheric entry, which occurs at the time labeled 0.00 in Fig. 8b and ends at landing, which occurs at some later time. The figure depicts three tracking scenarios.

1. DSN Tracking Only

DSN tracking, which includes two-way Doppler, range, and delta differential one-way ranging (ΔDOR) from DSN stations located at Goldstone, Madrid, and Canberra is represented by the solid line in Fig. 8. This level of support provides 24-h coverage. The data cutoff is at 6 h before entry, which is nominal for the MSL. After data cutoff, the trajectory error stays constant and simply maps forward in time until landing because of the effect of gravity focusing. Gravity focusing involves a trade in the error, in which the position errors reduce slightly whereas the velocity errors grow as the spacecraft falls into the gravity well. Since the mapping is symplectic, the phase volume of the 6-D error hyper ellipsoid remains constant.

The error growth during EDL is due almost entirely to the stochastic drag, which has been modeled at a level of 35% uncertainty (1σ) applied every 5 s and results in a 20-km (3σ) semimajor axis error at landing. The other significant result is the error at the 125-km altitude atmospheric interface, which is approximately 2.4 km (3σ) and differs slightly from the anticipated MSL delivery error of approximately 1.5 km (3σ). The difference between the result in Fig. 8 and the MSL estimate occurs because the simulation uses only 30 days of tracking data, whereas the MSL simulations routinely use 45-day arcs. Before moving on to the next result, it should be noted that the MSL's hypersonic guidance will fly to a nominal drag profile using its dead-reckoned IMU data to maintain trajectory knowledge. MSL analysis has suggested that the IMUs can maintain trajectory knowledge at the level of the entry error with a small growth to the order of a few hundred meters [4]. Indeed, the MSL's expected 3σ knowledge error at parachute deploy is expected to be around 2.1 km. Hence, even though Fig. 8 illustrates an error growth, it is expected that the MSL would maintain trajectory knowledge in practice using its accelerometers with error growth on the order of hundreds of meters.

2. DSN Tracking and MRO Tracking with a Six-Hour Data Cutoff

This scenario builds on the first scenario, except now there is two-way Doppler data being collected between the MSL and the MRO. The data starts at about 10 h before entry and is cut off at 6 h before entry. In the event that the MRO has to point its nadir deck to get the data, it can do so for 30 min at a time before batteries get low and it needs to reorient to collect solar energy. The 4-h period results in three passes of data. Note that atmospheric effects are not important since none of the observations are processed at low enough elevations. The case represents a scenario in which the Mars Network data could be telemetered back to Earth and processed with the DSN data to provide a knowledge update to the guidance system before atmospheric entry. Even this small amount of tracking indicates the value of the Mars Network-based Doppler tracking data. Indeed, the uncertainty at the top of the atmosphere has decreased to less than 230 m (3σ). The result displays the utility of using Mars Network-based tracking data to improve Mars-relative trajectory knowledge, even if it is not processed onboard and in real time. Again, the error growth during EDL is a result of stochastic drag. (The initial sharp drop in error at about -0.02 h after atmospheric entry is most likely because of a change in the atmospheric density corresponding to a layer transition in the model combined with gravity focusing and should be disregarded.)

3. DSN Tracking and MRO Tracking Until Landing

This case differs from the previous scenario in that tracking persists past the 6 h period and is continuous in the last 30 min, including the EDL phase. This results in six tracking passes between the MRO and the MSL. In this case, it is assumed at some point, the in situ data would be processed onboard by Electra and in real time to provide navigation updates. The results vividly display the benefit of the in situ Doppler, even during EDL. At atmospheric interface, the solution is better than 10 m (3σ) and grows slightly during atmospheric flight to about 100 m (3σ) at landing. Note that this case uses a slightly different MRO tracking schedule than the previous case with a 6 h data cutoff. For the case with a 6 h data cutoff, the final pass starts earlier than the same pass for the case with tracking until landing. The result is that the dashed line, corresponding to the 6 h data cutoff case, dips slightly below the dotted line, corresponding to the case of tracking until landing, until such time that tracking stops on the 6 h data cutoff case and continues with the other.

It should be emphasized that a key error source not included in the result is the map-tie error, relating knowledge of the inertial frame to the Mars body-fixed frame. Current estimates place the map tie error at around 450 m (3σ) [21]. Hence, the landed error in the example related to the Mars surface map is at this level. Additionally, dynamic flight with a lifting trajectory and parachutes are not included in the simulation; these will affect the performance of navigation with the in situ Doppler data.

B. EDL Navigation Performance

A covariance analysis for just the EDL portion of the MSL trajectory was also performed. The analysis includes DSN radiometric data collected starting 45 days before entry and ending 6 h before entry, which is the assumed data cutoff for the final onboard state update before entry. The resulting uncertainties from the approach navigation process are mapped to cruise stage separation, defined for the purposes of the study to be 10 min before entry-body atmosphere interface. The covariance matrix for the spacecraft position and velocity at entry interface were supplied as inputs to the beacon navigation analysis initial conditions [9].

The assumption used for the study is that spacecraft-to-spacecraft radiometric data collection starts at cruise stage separation. Results with simulated uhf data were created using a full 6×6 a priori covariance matrix from the approach navigation analysis with DSN data. The DSN covariance matrix represents the covariance for the estimated states and is a reasonable representation of the covariance analysis results from the MSL. Other parameters include uncertainty in the orbiter ephemeris and spacecraft clock errors. The results are shown in Figs. 9 and 10, for both position and velocity estimation errors and 1σ uncertainty bounds as a function of time relative to atmospheric entry. The uncertainties are reported in radial-transverse-normal (RTN) coordinates, defined as

$$\mathbf{R} = \frac{\mathbf{r}}{|\mathbf{r}|}, \qquad \mathbf{N} = \frac{\mathbf{r} \times \mathbf{v}}{|\mathbf{r} \times \mathbf{v}|}, \qquad \mathbf{T} = \mathbf{N} \times \mathbf{R} \tag{35}$$

where $\mathbf{r}$ and $\mathbf{v}$ are the inertial spacecraft position and velocity, respectively.

The current state estimation errors and 1σ uncertainty plots for the position components and a root-sum square (RSS) of all the elements is shown in Fig. 9. Each time history starts shortly before the start of uhf tracking at 10 min before atmospheric entry and extends for 2 min past entry interface. It is expected that the link will be interrupted by plasma between 1 and 2 min after entry, based on the EDL trajectory and telecommunications link analysis, and so the filter results are only presented to 2 min after entry. The most interesting aspect of the results is the rapid reduction in the uncertainties when the uhf data collection begins. The RSS error drops from nearly 800 m to under 200 m in 1 min, with a nearly linear decrease to well under 100 m by entry interface, defined as $t = 0$ in the figure, and steady error performance after entry interface. These results clearly show the benefits of collecting spacecraft-to-spacecraft uhf Doppler data and processing with a fit covariance from DSN radiometric data processing.

The current state estimation error and 1σ uncertainty plots for the velocity components and an RSS of all three velocity elements are shown in Fig. 10. The velocity shows a similar trend to the position, with large improvements to the uncertainties immediately after uhf data processing begins at 10 min before atmospheric entry. After less than 1 min of data processing, the velocity RSS error drops nearly a factor of 3, with smaller continued improvement as compared with the position error but continued improvement after entry interface.

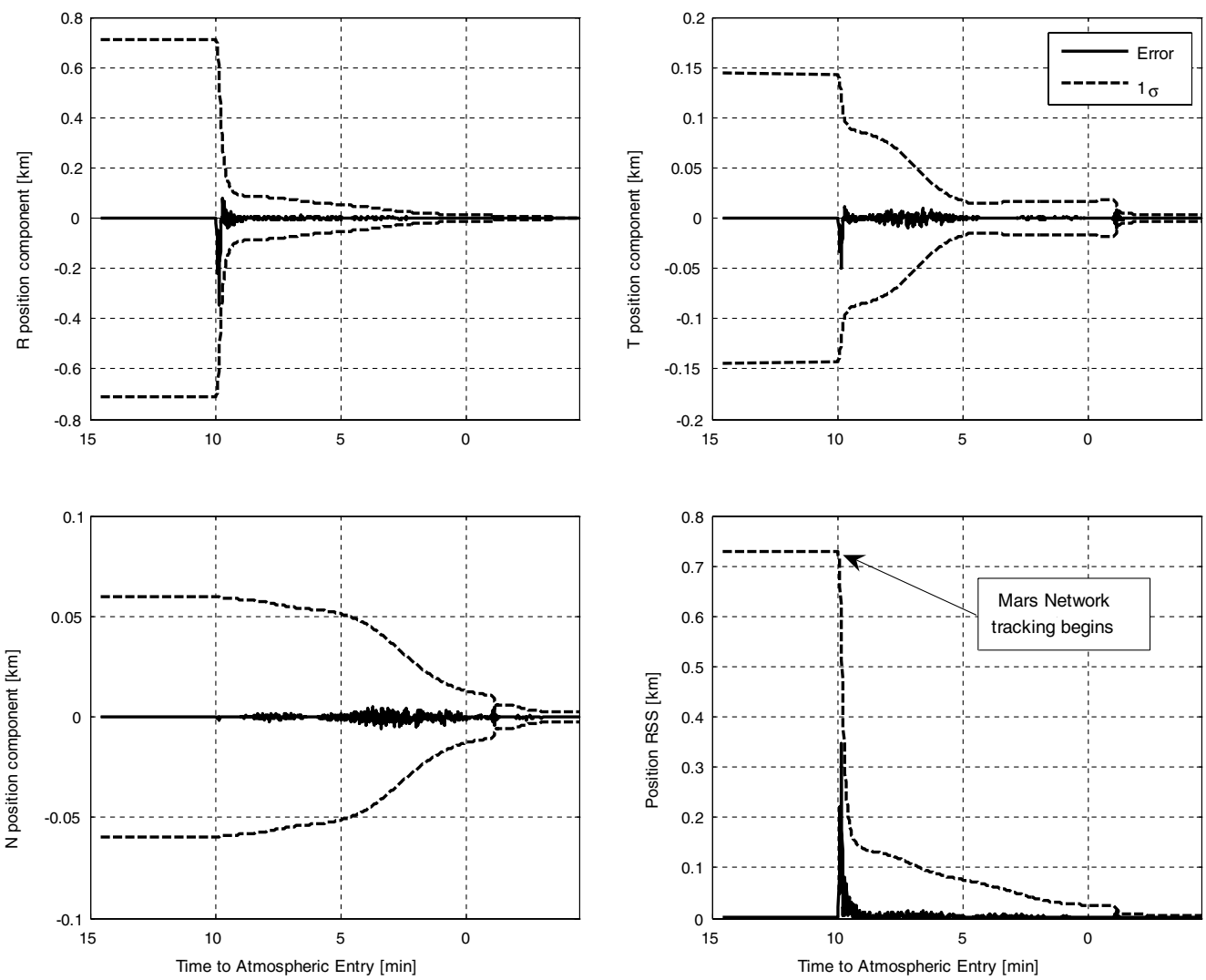

Fig. 9 Position estimation errors and 1σ uncertainty bounds for simulated uhf data processing with DSN tracking to 6 h before entry, and focusing on the last 15 min before entry.

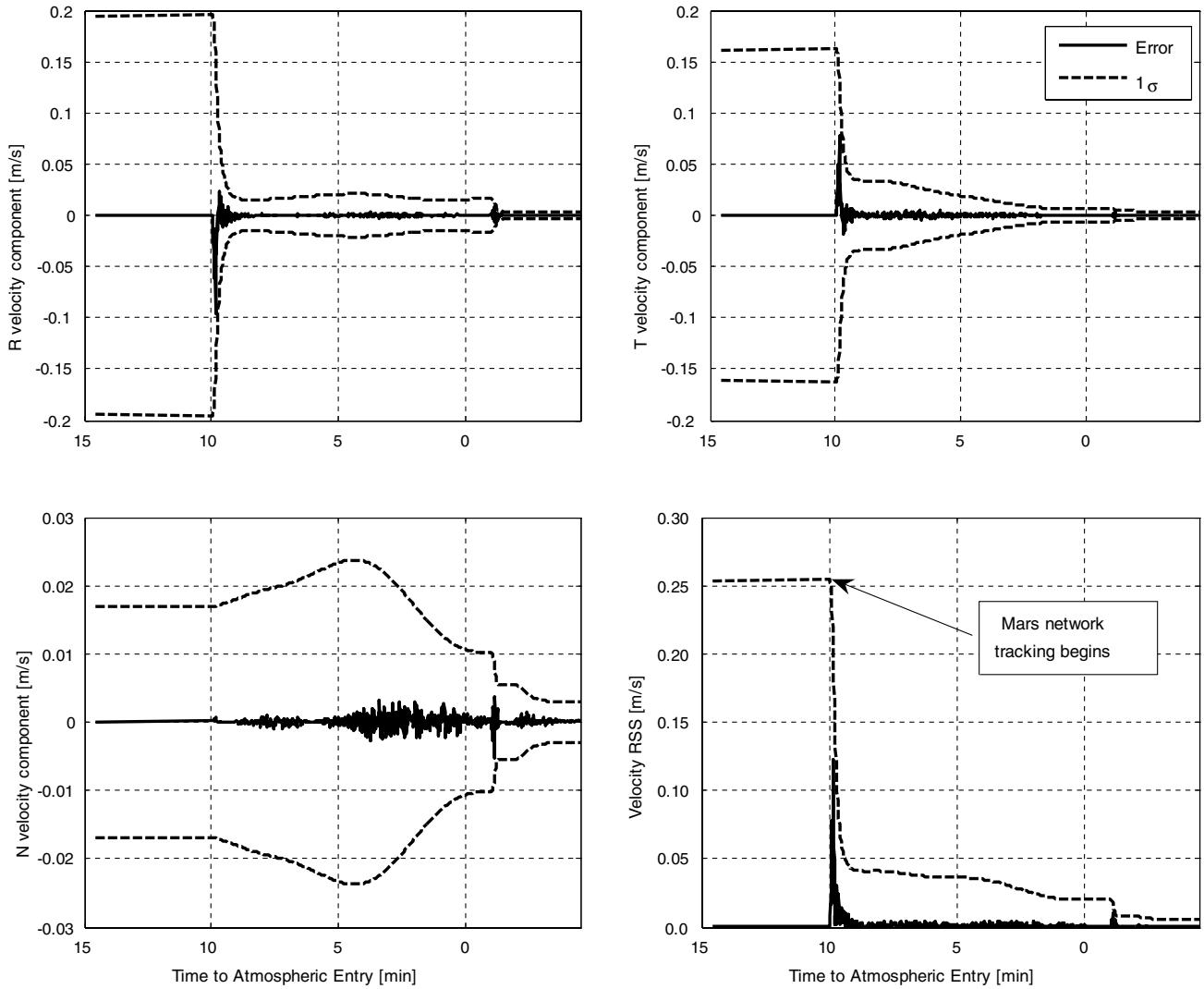

Fig. 10 Velocity estimation errors and 1σ uncertainty bounds for simulated uhf data processing with DSN tracking to 6 h before entry, focusing on the last 15 min before entry.

The preceding simulation results provide a basis for comparison with the real-time navigation software that was developed for the Electra. Ultimately, the high-fidelity simulation will generate the truth data that will drive the Electra prototype flight software.

VI. Algorithm Implementation and Run-Time Performance

The final goal of the task is to demonstrate the implemented algorithms processing data on the Electra engineering development unit (EDU). To reach the goal, a three-step implementation process was used. The simulation results discussed earlier were precursors to the implementation process, but the results generated served as the baseline for the navigation performance. Areas of similarity and difference in the measurement models, the filter strategy, and the implementation process between the approach navigation, EDL navigation, and EDL adaptive navigation work areas are described in Table 5.

The first step was to implement the algorithms in a stand-alone filter. Even though the step was free of any hardware constraints, coding practices consistent with the limitations of the final platform were enforced. These include language and processor speed limitations that require implementation of small and fast algorithms. Even though enforcing these restrictions on the stand-alone filter resulted in some development issues on commodity hardware, the result was an implementation that was similar to the final software but that used a more diverse suite of optimization and debugging tools than were available for the target processor. With a standard desktop computer, the implemented algorithms execute many times faster than real time, allowing more iterations and testing.

The second step was to execute the filter using an emulator of the Electra processor. The emulator provided a platform that was nearly

Table 5 Comparison of Electra analysis elements that are part of the advanced EDL work area

	Approach	EDL	Adaptive filtering
Measurement models	Doppler	Doppler, IMU	Doppler, IMU
Filter strategy	Factorized EKF using common libraries		EKF, Sigma-point filter using common libraries
Emulation	Linux-based RTEMS/SPARC CPU with C++ software. MATLAB-based emulation of Electra radio		Linux-based RTEMS/SPARC CPU with C++ software
Electra	Commercial parts version of Electra digital baseband processing module		

the same as the final hardware target while having more diagnostic output options than the hardware. The emulator also can be run much faster than real time and gives estimates of hardware performance that are reasonable estimates of the performance on the target hardware. Use of an emulator allowed the analysts more executions of the code and further insight into the execution of the implemented algorithms than was possible with the hardware, in addition to providing an alternative to using the hardware for every test. This allowed a majority of the testing to be performed in the emulator with less frequent but more productive testing with the hardware. The implementation required for the navigation filter on the emulator included not only the filter itself, but the input interface, data buffering, output interface, and housekeeping functions of the Electra EDU. The goal was to be able to build an executable that runs in the emulator and required no modification to run on the hardware. Navigation performance was evaluated here and compared with the stand-alone results. In addition, the run time of the navigation algorithms was determined, and any speed issues were addressed at this stage.

The final step was execution on the Electra EDU. Care was taken to minimize the amount of modification to go from step two to step three; in reality, there were minor differences between the emulator and the Electra EDU that required modification of the navigation and associated software. Once these modifications were made and the filter was operational on the Electra EDU, similar navigation performance and processing speed analyses were performed.

Although the first two steps performed were useful for implementation of the final filter, the results of interest were the performance on the Electra EDU. Intermediate results are not presented, specifically because these results must match the results of the hardware execution. The parameter of interest here is the execution speed of the algorithms in the Electra EDU relative to real time.

A. Electra Hardware

Software verification and performance testing are carried out on an actual Electra baseband processor module (BPM) to demonstrate compatibility with and suitability for the Electra computing environment. The Electra BPM is a rack-mounted unit constructed from commercial parts and includes the SPARC processor, the memory, the I/O with all support logic, and the signal-processing, field-programmable gate array (FPGA). No uhf downconverter is included, but the unit does support signal processing at the Electra 71 MHz intermediate frequency. The primary user interface to Electra is a local PC running a custom LabVIEW package. The package is used to load and retrieve software and data, to interact with that software, and to interact with the Electra monitor program residing in boot PROM. The BPM SPARC V7 CPU runs at 24 MHz and is supported by a 1 Mbit boot PROM, 16 Mbit of EEPROM, 16 Mbit of SRAM and 256 Mbit of error detection and correction (EDAC) synchronous dynamic random access memory (SDRAM), of which 170.5 Mbit, or 67%, is available for mass data storage. Interfaces supported include serial (RS-232), IEEE-1553, and low-voltage differential signaling (LVDS) for high-speed direct memory access (DMA) transfers.

B. Electra Navigation Software

The SPARC software consists of several tasks that run under the Real-Time Executive for Multiprocessor Systems (RTEMS) version 4.0.0 in a single-processor mode. A public domain SPARC RTEMS development environment that includes a Linux-hosted software simulator is used for development. This product, circa 1998, uses GNU development tools (g++ version egcs 2.91.66, gdb 4.17.gnat.3.11p, etc.) and an ERC32 GNU cross compiler. To maintain both compatibility with the Electra radio software work and a target of a joint radio and navigation software load for an operational Electra, this package was used for the Electra navigation (ElectraNav) demonstration work. Electra personnel have upgraded these tools, and ElectraNav plans to follow suit.

Navigation algorithms are computationally intensive, and so the purpose of the demonstration is to show that meaningful navigation results can be obtained within the SPARC V7 24 MHz computing environment, ultimately with enough spare resources to allow coexistent operation with the Electra radio software. The Furies Filter, version 3.0, is the current navigation filter application under test in the environment. It has simulated inputs in the form of Electra-integrated Doppler and IMU measurements. The Electra filter can process these data as they arrive, or an intelligent accumulation can be performed by correcting the accelerometer output, based on the computed vehicle attitude, to reduce the number of data processing steps. The rates under investigation vary from 10 Hz to 0.1 Hz. The 0.1 Hz rate is consistent with the expected Doppler rate.

The nominal state is propagated by a Runge–Kutta fourth-order integrator with adjustable step size (RK4–5). Integration is evaluated using the adjustable step size, and the step size is fixed at a reasonable value for the test regime to save integration time. Both the approaching spacecraft and the Mars Network orbiter are integrated in the modeling process. During integration, partial derivatives are also computed using the chain rule in parallel with the calculations used to model physical reality. This makes partial derivatives with appropriate time references available for filter time and measurement updates. The integrator is to be extended with a spline algorithm to save processor time for interpolated state and partial derivative values.

Filter covariance is processed in UDU-factorized form for greater numerical stability. Whereas the use of a factorized filter is not required for the EDL navigation problem, the computational impact of using a factorized filter only appears at initialization and for output, in which conversion to standard metric units from a factorized form is required. All filter processing is done with the factorized matrices [18]. Integrated Doppler measurements are corrected for both vehicles' travel during the light-time propagation. The Mars gravitational-mass constant, planetary rotation, and an exponential atmosphere are included in the models currently under test. These models are all extensible. For example, the atmosphere model may be increased to multiple exponential layers, the gravity model may be increased in degree and order, and relativity may be added to the light-time and other models.

A high-fidelity model of the approach is used as truth for algorithmic validation and test comparison and for the generation of test observables. As work progresses, the intent is to refine models in ElectraNav to give acceptable agreement with the truth without exceeding resource limits, particularly CPU usage.

The implemented navigation filter has slightly over 14,000 lines of code with an image size of 1.328 MB, both well within the capacity of the hardware. The performance for a 12-state model, which includes position and velocity for both the approaching spacecraft and the Mars Network orbiter, is shown in Table 6. These results are preliminary and correspond to a 75 s integration time, with integrated Doppler measurements every 10 s and IMU measurements at various rates. The next steps to be carried out in a follow-up task to this effort include additional optimization and some additional model improvements, including adding clock parameters to the state and

Table 6 Electra navigation filter performance for varying IMU data rates with a 12-state model, processing 10 s Doppler measurements for 75 s and varying IMU data rates

Case	Software emulator	Hardware	% real time	Notes
1 IMU	29 s	70 s	93	No IMU data
70 IMU	32 s	80 s	107	One IMU data point per second
790 IMU	67 s	170 s	227	10 IMU data points per second

estimate lists. While thought was given to performance in the current implementation, the focus to date has been computational correctness. This balance will shift more to meeting the computational performance targets as the code matures. For example, direct integration of the orbiter trajectory and partials can be replaced by Keplerian elements, which saves processor time and retains precision. The expectation is that, if the navigation software of suitable algorithmic fidelity and stability can operate in the single process mode in 30–50% of real time, it will be able to coexist with the radio software under RTEMS in real time. This level of performance appears to be within reach.

VII. Conclusions

This paper described a technology task that is developing an embedded, real-time navigation system for Mars final approach and EDL using the Mars Network's Electra uhf transceiver. A set of analyses based on the 2010 encounter at Mars between the MSL and the MRO spacecraft demonstrated that the Electra link can be closed at a range of approximately 110,000 km, corresponding to 10 h before atmospheric entry. It was further demonstrated, through high-fidelity simulations and covariance analyses, that the navigation system is capable of achieving 300-m or better atmosphere entry knowledge error and that the resulting technology is enabling for pinpoint landing. Finally, the paper presented a detailed development of the navigation algorithms, including the dynamic models and the measurement models, and described the three-step implementation process for demonstrating the run-time performance of the navigation filter running on actual Electra hardware.

Acknowledgments

This research was carried out at the California Institute of Technology (JPL) Jet Propulsion Laboratory and at The University of Texas at Austin. The work was funded by the Mars Technology Program under JPL contract numbers 1264090 and 1264119. Reference herein to any specific commercial product, process, or service by trade name, trademark, manufacturer, or otherwise does not constitute or imply its endorsement by the United States Government or the Jet Propulsion Laboratory, California Institute of Technology.

References

[1] "Solar System Exploration," NASA Office of Space Science, Jet Propulsion Laboratory, 400-1077, Pasadena, CA, May 2003.

[2] Bell, D. J., Cesarone, R., Ely, T. A.,Edwards, C., and Townes, S., "Mars Network: A Mars Orbiting Communications & Navigation Satellite Constellation," *IEEE Aerospace Conference* IEEE Publications, Piscataway, NJ, 18–25 March 2000, pp. 75–88.

[3] Hastrup, R. C., Bell, D. J., Cesarone, R. J., Edwards, C. D., Ely, T. A., Guinn, J. R., Rosell, S. N., Srinivasan, J. M., and Townes, S. A., "Mars Network for Enabling Low-Cost Missions," *Acta Astronautica*, Vol. 52, No. 2, Jan. 2003, pp. 227–235. doi:10.1016/S0094-5765(02)00161-3

[4] "Mars Program Pinpoint Landing System Study," Jet Propulsion Laboratory, Pasadena, CA, 2003.

[5] Edward, C. D., Adams, J. T., Bell, D. J., Cesarone, R., Depaula, R., Durning, J. F., Ely, T. A., Leung, R. Y., McGraw, C. A., and Rosell, S. N., "Strategies for Telecommunications and Navigation in Support of Mars Exploration," *Acta Astronautica*, Vol. 48, No. 5, March–June 2001, pp. 661–668. doi:10.1016/S0094-5765(01)00042-X

[6] "Mars Relay Description for Scout Proposals," NASA Langley Research Center, Hampton, VA, 24 April 2006.

[7] Ely, T. A., "Mars Network Radiometric Measurement Models and Data Interfaces for the Electra and CE-505 Radios," Jet Propulsion Laboratory, IOM Electra-343K, Pasadena, CA, Oct. 2006.

[8] Jai, B., Wenkert, D., Halbrook, T., and Sidney, W., "The Mars Reconnaissance Orbiter Mission Operations: Architecture and Approach," AIAA Paper 2006-5956, June 2006.

[9] Burkhart, P. D., *Approach Navigation for the 2009 Mars Large Lander*, Advances in the Astronautical Sciences, Vol. 114, Univelt, San Diego, CA, 2003, pp. 2183–2198.

[10] Mendeck, G. F., and Karman, G. L., "Guidance Design for Mars Smart Landers Using the Entry Terminal Point Controller," AIAA Paper 2002-4502, 5–8 Aug. 2002.

[11] Wolf, A., Tooley, J., Ploen, S., Gromov, K., Ivanov, M., and Acikmese, B., "Performance Trades for Mars Pinpoint Landing," *Proceedings of the IEEE Aerospace Conference*, IEEE Publications, Piscataway, NJ, 4–11 March 2006.

[12] Lightsey, E., Campbell, T., Mogensen, A., Burkhart, P. D., Ely, T., and Duncan, C., "Expected Performance of the Electra Transceiver for Mars Missions,"AIAA Paper 2005-5948, 15–18 Aug. 2005.

[13] Satorius, E., and Jedry, T., "DTTL Lock Detector, SNR Estimator, and Viterbi Sync Detection," Jet Propulsion Laboratory, Interoffice Memorandum, Pasadena, CA, 12 April 2004.

[14] Lisano, M., "Interim Planetary Atmosphere Navigation for Estimation and Mission Analysis (IPANEMA) Algorithm Design Document, Version 1.0," Jet Propulsion Laboratory, Pasadena, CA, June 2002.

[15] Jah, M. K., Lisano, M. E., Born, G. H., and Axelrad, P., "Mars Aerobraking Spacecraft State Estimation by Processing Inertial Measurement Unit Data," NASA Paper 2005–213901, Aug. 2005.

[16] Gelb, A., *Applied Optimal Estimation*, MIT Press, Cambridge, MA, 1992.

[17] Carlson, N. A., "Federated Square Root Filter for Decentralized Parallel Processes," *IEEE Transactions on Aerospace and Electronic Systems*, Vol. 26, No. 3, 1990, pp. 517–525. doi:10.1109/7.106130

[18] Bierman, G. J., *Factorization Methods for Discrete Sequential Estimation*, Academic Press, New York, 1977.

[19] Julier, S. J., and Uhlmann, J. K., "A New Extension of the Kalman Filter to Nonlinear Systems," *Proceedings of SPIE—The International Society for Optical Engineering*, Vol. 3068, SPIE–International Society for Optical Engineering, Bellingham, WA, April 1997, pp. 182–193.

[20] Heyne, M. C., and Bishop, R. H., "Spacecraft Entry Navigation Using Sigma Point Kalman Filtering," *Proceedings of the IEEE/ION Position, Location and Navigation Symposium*, IEEE, New York, 25–27 April 2006, pp. 71–79.

[21] Li, R., Squyres, S. W., Arvidson, R. E., Archinal, B. A., Bell, J., Cheng, Y., Crumpler, L., Des Marais, D. J., Di, K., Ely, T. A., Golombek, M., Graat, E., Grant, J., Guinn, J., Johnson, A., Greeley, R., Kirk, R. L., Maimone, M., Matthies, L. H., Malin, M., Parker, T., Sims, M., Soderblom, L. A., Thompson, S., Wang, J., Whelley, P., and Xu, F., "Initial Results of Rover Localization and Topographic Mapping for the 2003 Mars Exploration Rover Mission," *Photogrammetric Engineering and Remote Sensing*, Vol. 71, No. 10, Oct. 2005, pp. 1129–1142.

C. Kluever
Associate Editor